Biomedical Signal Processing and Control 87 (2024) 105484

Contents lists available at ScienceDirect

Biomedical Signal Processing and Control

journal homepage: www.elsevier.com/locate/bspc

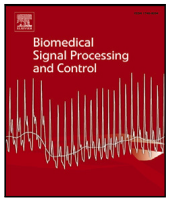

High accurate detection method for aortic valve opening of seismocardiography signals☆

Chundi Zheng [a,*], Weiming Peng [b], Tianyao Huang [c], Yonina C. Eldar [d], Meiyi Yu [b]

[a] School of Electronic Information Engineering, Foshan University, Foshan, 528225, Guangdong, China
[b] School of Mechatronic Engineering and Automation, Foshan University, Foshan, 528225, Guangdong, China
[c] School of Computer and Communication Engineering, University of Science and Technology Beijing, Beijing, 100083, China
[d] Faculty of Mathematics and Computer Science, Weizmann Institute of Science, Rehovot, 7610001, Israel

ARTICLE INFO

Keywords:
Seismocardiography (SCG)
Heart rate estimation
AO peak estimation
Heartbeat detection
Vital sign monitoring

ABSTRACT

Accurately detecting the aortic valve opening (AO) peaks of seismocardiography (SCG) is a challenging problem due to interference of other morphological inflection points. In this paper, a high accurate method is proposed to extract AO peaks based solely upon the SCG data. The raw SCG signal is purified by a simple first order interference cancellation method, resulting in a reduced number of modes to be decomposed. The purified SCG signal is then decomposed into a series of quasi-orthogonal modes by successive variational mode decomposition (SVMD) without any prior about the number of modes. Considering the pulsatile nature of the AO signal, a waveform factor criterion is proposed to reconstruct the AO signal based on the pulsatile level of each mode. A seventh power law detector is designed to amplify the AO peak and suppress spurious peaks. The publicly available combined measurement of electrocardiogram (ECG), breathing and seismocardiograms (CEBS) database is exploited to verify the performance of the proposed method. We show that the average sensitivity of our technique is 99.02%, the prediction rate is 99.06%, and the detection accuracy is 98.10%, which is superior to several state-of-the-art methods. In addition, compared with the ECG reference value, the instantaneous heart rate extracted by the proposed method is in good agreement with that of the ECG, e.g., the maximum average absolute error percentage is as low as 2.11 and the maximum average value relative error is about 0.03, further demonstrating that the proposed method can achieve accurate estimates of heart rate with an accelerometer alone.

1. Introduction

Heart disease is considered to be one of the leading causes of human death [1–4]. Studies have shown that changes in heart rate are closely related to cardiac condition [5]. Therefore, real-time monitoring of heart rate variation in daily life is very important for early detection of hidden heart disease. ECG has been widely used to detect changes in electrical activity caused by cardiac activity. However, more recently, benefited from the fast development of sensor technology, SCG [4,6], ballistocardiography (GCG) [7], kinocardiography (KCG) [8], and forcecardiography (FCG) [9–11] have received great attention. In particular, SCG uses a small high-precision acceleration sensor to measure the acceleration of the chest wall movement caused by heartbeat, and provides a new convenient, inexpensive, and efficient way for heart rate monitoring in daily life [4,12].

The advantages of SCG over ECG are multi-fold. First, SCG better identifies the clinical diagnostic information corresponding to the mechanical activities of the heart [13], while ECG based on electrical activity measurements may fail to detect those structural defects. These mechanical activities include the motion state of the heart valve, the state of ventricular blood circulation, the state of ventricular wall, and more [14]. Second, SCG provides a non-invasive way for diagnosis by simply sticking a small acceleration sensor to the chest wall. SCG is also more suitable for critical and emergent cases, because the acceleration sensor is easier to install and deploy compared to preparing electrode connections [15]. Finally, due to its simplicity, SCG has the potential to embed into smart phones to realize intelligent medical monitoring anytime and anywhere in the near future [16]. Therefore, the SCG prospects are elated for applications in daily health monitoring and promotion of heart disease prevention.

The morphology of SCG signals reveals different types of heart motions and thus health conditions. A cardiac cycle can be divided into systolic and diastolic phases. Cardiac motion changes significantly at

☆ This work was supported by special scientific research funding project of Department of Education of Guangdong Province of China (2020KZDZX1206).
* Corresponding author.
E-mail addresses: cdzheng@fosu.edu.cn (C. Zheng), huangtianyao@ustb.edu.cn (T. Huang), yonina.eldar@weizmann.ac.il (Y.C. Eldar).

https://doi.org/10.1016/j.bspc.2023.105484
Received 2 September 2022; Received in revised form 4 September 2023; Accepted 12 September 2023
Available online 29 September 2023

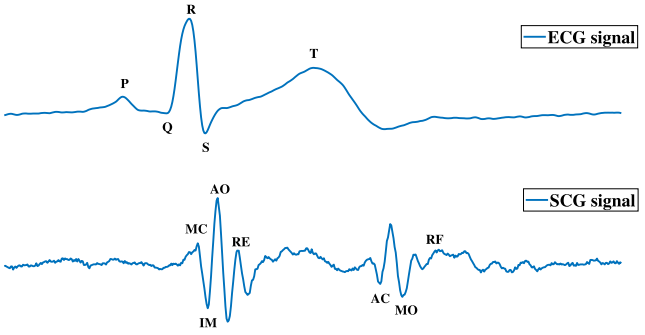

Fig. 1. Synchronised ECG (above) and SCG (below) records from the CEBS database.

the two phases due to changes in volume and pressure, which gives rise to a rhythmic pulsation in the chest for each beat of the heart [17]. The main benchmarks associated with the systolic and diastolic phases are AO, aortic valve closure (AC), isovolumic moment (IM), mitral valve opening (MO), mitral valve closure (MC), rapid blood filling (RF), and rapid ejection (RE) [12,14,18], which can be revealed by the rhythmic cardiac acceleration signals, as shown in Fig. 1.

Among all these benchmarks in a SCG cycle, the AO point is the most critical inflection point of the systolic profile, which is used to estimate the beat-to-beat systolic time interval [12,19,20]. The average AO-AO interval in one-minute SCG signal can evaluate the number of beats per minute. Furthermore, it can also be used for diagnostic analysis, such as heart rate variability analysis [21,22]. Consequently, AO point detection plays an important role in heart health monitoring [23]. Incidentally, recent study has shown that the template matching method can provide very accurate estimates of the heartbeat interval without having to localize any specific SCG peak [24].

These AO peaks can be annotated manually, but it is generally quite time-consuming. Recent works consider automatic extraction of AO peaks [13,25]. However, this is a non-trivial problem due to noise-contaminated measurements and other interference [13,20]. The use of multiple sensors facilitates AO peak estimation. For example, many works utilize an ECG signal as Ref. [21,26,27], which better indicates the characteristics of SCG signals, but it is inconvenient for routine monitoring. An alternative is to combine a gyroscope or an extra accelerometer [28,29], which alleviates motion noise. But these devices undoubtedly increase the complexity and cost of the system.

There have also been many signal processing efforts devoted for AO peak extraction from a single sensor, which is our focus here. one of the main challenges is how to extract the AO peak under the interference of the non-AO morphological inflection points. Unlike the ideal case in Fig. 1 where the AO peak dominates the other surrounded inflection points, in many practical noisy scenes, the AO peaks are not the most prominent ones [30]. Although the non-prominent AO peaks can be identified according to the morphological characteristics of SCG signals by manual annotation or ECG assist, these approaches are inefficient and expensive.

Considering that the SCG signal is composed of multiple sub-signals, an effective approach is to first decompose it into a series of modes and then reconstruct the desired AO signal by mining the underlying modal information. Several classical signal decomposition techniques have been employed to extract the AO signal from fundamental components with inherent properties. See [31] for a detailed analysis of the advantages and disadvantages of this approach. Siecinski et al. [32] applied empirical mode decomposition (EMD), which is sensitive to noise due to its recursive property [31]. To enhance the robustness against noise, Choudhary et al. [33] employed variational mode decomposition (VMD) [34] to decompose the SCG signal, in which a single IMF component is empirically selected in term of the oscillation amplitude to construct the heart rate envelope. However, selecting only one IMF component may miss important heartbeat information in some SCG signals [35–37]. To overcome the information loss of the single IMF, [35] exploited two modes. In addition, the authors proposed the modified VMD (MVMD) algorithm, which improves the accuracy of AO peak estimation, at the cost of increased complexity since it relies on two stage VMDs. A common drawback of existing EMD, VMD, and MVMD methods is that they require setting the proper number of modes in advance, otherwise the final heart rate results are severely affected [38]. Another open issue is how to efficiently choose suitable modes to reconstruct the AO signal from the numerous IMF components [13,35].

To address the above issues, we apply SVMD, which does not need the number of modes as input but estimates the number automatically. Being aware of the pulsatile nature of the AO signal, we propose the waveform factor to evaluate the pulsatile level of each IMF component and use the result as the criterion to select IMFs for AO signal reconstruction. In addition, we also propose preprocessing of the raw SCG signal prior to the decomposition, which purifies the SCG signal and enhances the decomposition and reconstruction quality. Based on the reconstructed AO signal, we propose a computationally efficient method to extract and smooth the envelope, which yields accurate detection of AO peaks. We summarize the main contributions as follows:

(1) *Preprocessing the raw SCG signal*: Instead of directly decomposing the raw SCG data, we construct filters to cancel out-band artifacts, which improves the performance of the subsequent signal decomposition in two aspects: The number of output modes is reduced, alleviating the computational complexity, and more importantly facilitating the follow-up mode selection. These filters are designed by applying MTI techniques widely used in radars [39,40], which perform well for SCG signals and are simple to implement.
(2) *Decomposing the SCG signal without a prior on the number of modes*: After preprocessing, SVMD [41] is employed to decompose the SCG signal without knowing the number of modes, which avoids estimation error caused by improper number of modes selection. SVMD solves a series of one-dimensional problems accompanied by a reduced number of modes, resulting in low computational complexity.
(3) *Waveform factor criterion*: Once the SCG signal is decomposed into several IMF components by SVMD, a criterion is essential for choosing which components best represent the AO signal. The overestimated number of components will cause a large number of non-AO signals, while an underestimated number might result in missing AO peaks. The proposed waveform factor criterion, which exploits and evaluates the intrinsic pulsating character of AO signals, empirically shows enhanced capacity in selecting desired modes.
(4) *Envelope extraction and smoothing*: A seventh power law detector is designed to enhance the amplitude of the AO peak and simultaneously suppress the surviving non-AO peaks in the reconstructed AO signal, which yields a cleaner envelope and relieves spurious peaks.

Experimental data from a public dataset (CEBS) [42] shows that the proposed method not only provides more accurate heart rate estimates than several state-of-the-art methods but also enjoys lower computational complexity. In particular, our technique achieved average sensitivity of 99.02%, prediction rate of 99.06%, and detection accuracy of 98.10%. Compared with the instantaneous heart rate of the ECG reference value, our technique reduces the maximum average absolute error percentage and the maximum average value relative error to about 2.11 and 0.03, respectively.

The remainder of this paper is organized as follows. Section 2 introduces the signal model and the proposed method in detail, including preprocessing, signal decomposition and reconstruction, as well as AO peak position detection. Experimental results and discussions are provided in Section 3. Finally, conclusions are drawn in Section 4.

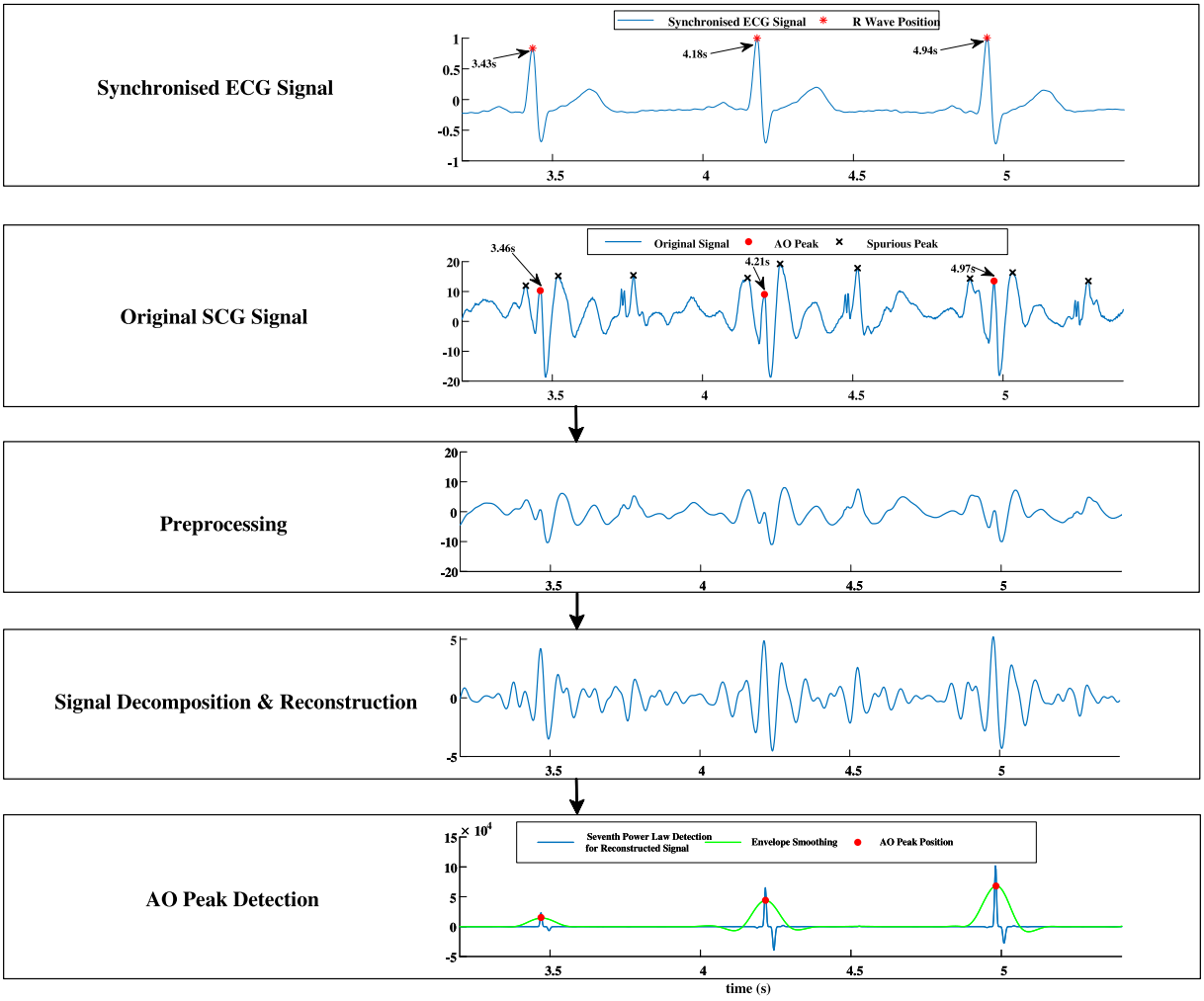

Fig. 2. The main processing flow of the proposed AO peak detection method (CEBS database recording: b008).

2. Model and methodology

In this section, we model the chest acceleration signal and introduce the signal processing flow.

2.1. Signal model

SCG measures the local vibrations of the chest wall induced by cardiac activity in a noninvasive manner; see original signal in Fig. 2 as an example of the measurements. The AO peaks in the measurements indicate many diagnostic information. Our goal is to detect these AO peaks efficiently from the measurements. This is non-trivial, because the original signals are contaminated, making the AO peaks submerged by spurious peaks.

The first challenge is that the signal collected from the accelerometer may be interfered by other vibrations, e.g., unavoidable breathing [13,43–45]. The SCG signal is often regarded as a superposition of several vibration signals, expressed as:

$$s(t) = s_{SCG}(t) + s_I(t), \tag{1}$$

where $s_{SCG}(t)$ and $s_I(t)$ are the SCG and interference signal, respectively. Therefore, the first task is to remove the interference signal from the measurements and purify the SCG signals at low computational cost. The interference signal from breathing has larger amplitude and lower frequency than the SCG signal [46]. Although the breathing masks the SCG signal in terms of the amplitude, its lower oscillation frequency allows us to filter it out by high-pass filtering.

Secondly, as is shown in Fig. 1, the morphology of the waveform of each cardiac cycle contains several inflection points that correspond to different mechanical events [13]. We then further write the SCG signal as:

$$s_{SCG}(t) = s_{AO}(t) + s_O(t), \tag{2}$$

where $s_{AO}(t)$ and $s_O(t)$ denote the AO signal and the other inflection point signal in SCG, respectively.

For example as shown in Fig. 2, some AO peaks are less significant than those of MC and RE peaks. As a result, it is crucial to identify the signal components corresponding to AO from other various subject morphology. As will be detailed later, this is the most critical challenge.

With the separated signal components due to AO, the last task is to calculate its envelope and identify the periodic peaks.

To overcome these challenges, we propose to exploit three key signal processing steps, and show their results in Fig. 2. The basic ideas of these steps are:

(a) *Signal preprocessing*: Since the desired AO signals are band limited, we construct a band-pass filter by subtracting the outputs of two high-pass filters with different cut-off frequencies to eliminate the respiratory interference and high-frequency noise, i.e., $s_I(t)$.
(b) *Signal decomposition and reconstruction*: This step aims to further extract AO signals out of the purified SCG signal, separating from other cardiac phases like MC and RE. Since the analytical expressions of these SCG morphology are difficult to obtain, we complete this step by heuristically decomposing the SCG signals

into a series of components. Observe the morphology of the SCG signal, the AO signals reveals a pulsating nature of the heartbeat. Then we select some of the components that represent the pulsating character to reconstruct the AO signals $s_{AO}(t)$.

(c) *AO peak position detection*: Given the reconstructed AO signal, this step calculates and smooths its envelop, and finally highlights positions of AO peaks.

These steps are explained in detail below.

2.2. Preprocessing

We perform time-domain filtering to remove the out-of-band interference/noise in $s_I(t)$.

The key ingredients of the concerned systolic profile are band limited. Therefore, we apply filters to remove the out-of-band interference/noise. Particularly, the desired signals are around 1 to 40 Hz [13,45,47–49]. The respiration interference generally has lower frequency than the heartbeat signal [44], and composes one of the main sources of the artifacts. In addition, the recommended sampling rate is well above 40 Hz [44], so high frequency noise above 40 Hz is also sampled and contaminates the raw data. These low and high frequency artifacts will be removed at low implementation costs.

The main procedure is the following:

- Form a band-pass filter via two high-pass filters, removing both the low-frequency respiration and the high-frequency artifacts in raw signal $s(t)$. These two high-pass filters have different cutoff frequencies, but the responses at frequencies higher than 40 Hz are almost identical. A subtraction operation of the outputs of the above two filters will remain the intermediate frequency between about 0.5 Hz and 14 Hz that corresponds to the desired SCG signal [50].

To construct the filters, we use the MTI technique from radar [39,40], in which returns from fixed or slow-moving unwanted targets (i.e., low-frequency signals) are rejected and signals from moving targets are displayed [51]. We regard the low-frequency respiration as the slow-moving unwanted target so that the MTI technique can be employed to remove it. The MTI filter is a first-order finite impulse response (FIR) filter, which first extracts the low frequency component, given by,

$$s_R(t) = \beta s_R(t-1) + (1-\beta)s(t), \tag{3}$$

and then subtracts it from the input, yielding the filtered output

$$x(t) = s(t) - s_R(t). \tag{4}$$

Here, $0 < \beta < 1$ is the weighting value, determining the cutoff frequency. The MTI is essentially a high-pass filter with transfer function $H(z) = (\beta - \beta z^{-1})/(1 - \beta z^{-1})$ [40].

Fig. 3 shows two examples of the magnitude responses of MTI filters, with β set to $\beta_1 = 0.9$ and $\beta_2 = 0.99$, respectively, and the sampling rate is 500 Hz that corresponds to the subsequent processing for the CEBS database.

We denote the outputs of two high-pass filters in (4) by $x^{\beta_1}(t)$ and $x^{\beta_2}(t)$, respectively. A subtraction yields:

$$y(t) = x^{\beta_2}(t) - x^{\beta_1}(t), \tag{5}$$

which suppresses high frequency noise.

Fig. 4 compares between the signals before and after the interference cancellation in the time and frequency domains, i.e., $s(t)$ and $y(t)$. As can be seen from Fig. 4(a), the fast-fluctuating component in the time domain that corresponds to the high frequency noise is eliminated after interference cancellation. The results in Fig. 4(b) also show that both low frequency artifacts and the high frequency noise are significantly eliminated.

There may be a residual trend component from the zero drift of the accelerometer [52] and spikes in the residual. The former could be detrended by the regression approach in [53] and the latter could be canceled by a fifth-order median filter in [13]. We label $y(t)$ followed by the detrending and median filtering operations as $s_{SCG}(t)$.

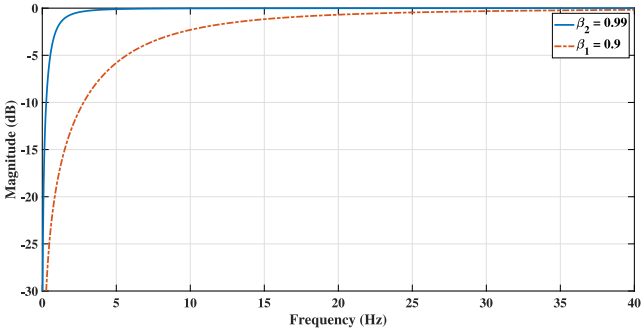

Fig. 3. Magnitude response of MTI filters for two different weighting values.

2.3. Signal decomposition and reconstruction

Although we obtained a cleaner SCG signal by preprocessing, the AO peaks are not necessarily significant enough to be detected, as shown in the second subplot of Fig. 2. The AO peaks are only a fraction of the systolic profile components of SCG [13], and may be masked by the stronger fractions. To reveal these AO peaks, it is essential to extract the fraction corresponding to the peaks from the original SCG signal.

While the exact motion models are unknown, the extraction is performed in a heuristic fashion [35]: (1) Decompose the original SCG signal into several modes; (2) Select a fraction of modes that has the notable pulsation character to reconstruct the AO signal. This procedure is represented by the following equations:

$$s_{SCG}(t) = \sum_{k=1}^{K} u_k(t) + \epsilon(t), \tag{6}$$

$$s_{AO}(t) = \sum_{m} u_m(t), \tag{7}$$

where $u_k(t)$ is the kth mode, K is the number of modes that compose the original SCG signal $s_{SCG}(t)$, $\epsilon(t)$ is the residual, and m denotes an index of selected modes to reconstruct the AO signal $s_{AO}(t)$.

Many previous works apply VMD [34] for signal decomposition. The main downside is that it heavily depends on the prior knowledge of the number of modes K, which is typically unknown in practice. How to identify modes that characterize the AO signal is another critical challenge.

In this paper, we propose to employ SVMD [41] (first developed for ECG signal processing) to decompose the SCG signal, which does not require K, and additionally reduces the computational load. Regarding the mode selection problem, we propose a criterion based on the pulsatile level to the identify whether each mode corresponds to the AO signal, which is simple to implement. In this subsection, we will introduce the SVMD method and the proposed criterion in the sequel, respectively.

2.3.1. Successive variational mode decomposition

VMD is an adaptive signal decomposition method [33,35], which can be regarded as a variant of Wiener filtering with Tikhonov regularization and augmented Lagrange [34]. Given K, VMD generates K modes at the same time by solving a constrained variational problem via alternate direction method of multipliers (ADMM) [54]. In contrast, SVMD extracts the modes successively [41], and terminates according to a certain condition, automatically providing an estimate of K. In addition, SVMD is computationally efficient, because it solves a series of one-dimensional problems, rather than a much more complex K-dimensional problem as VMD [55]. Here, we briefly introduce SVMD [41]. Without loss of generality, we assume that $s_{SCG}(t)$ is decomposed into two parts:

$$s_{SCG}(t) = u_k(t) + u_r(t), \tag{8}$$

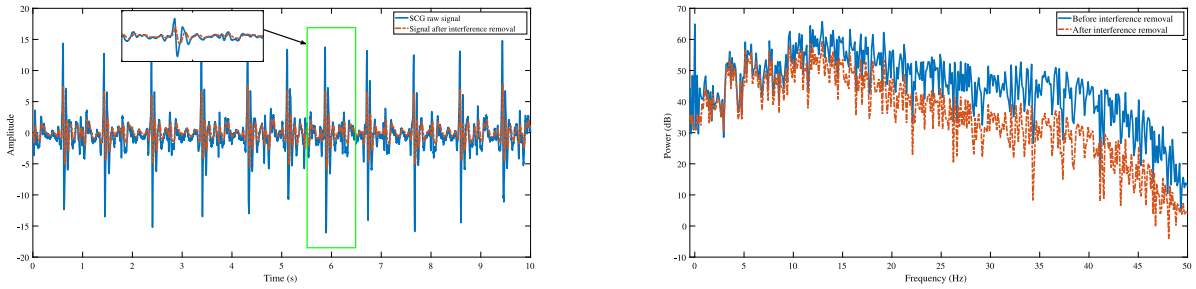

(a) Time domain (b) Frequency domain

Fig. 4. Comparison between signals before and after interference cancellation for b016.

where $u_k(t)$ is the kth mode and $u_r(t)$ is the rest of the signal which is written as:

$$u_r(t) = \sum_{i=1}^{k-1} u_i(t) + u_p(t), \tag{9}$$

where $\sum_{i=1}^{k-1} u_i(t)$ are the previously acquired modes and $u_p(t)$ is the unprocessed signals. SVMD was proposed in [41] based on the following four criteria:

(a) The kth mode minimizes the following metric:

$$J_1 = \left\| \partial_t \left[\left(\delta(t) + \frac{j}{\pi t} \right) * u_k(t) \right] e^{-j\omega_k t} \right\|_2^2, \tag{10}$$

where ω_k is the center frequency of the kth mode, the sign $*$, $\|\cdot\|_2$, and $\delta(t)$ denotes the convolution operation, the ℓ_2 norm, and the Dirac function, respectively; $j^2 = -1$.

(b) The spectral overlap between $u_k(t)$ and $u_r(t)$ is minimized by the following criterion:

$$J_2 = \left\| \gamma_k(t) * u_r(t) \right\|_2^2, \tag{11}$$

where $\gamma_k(t) = \frac{1}{\alpha(\omega-\omega_k)^2}$ is the impulse response of the filter.

(c) The kth mode should have the smallest energy leakage over the previously obtained modes by the following criterion:

$$J_3 = \sum_{i=1}^{k-1} \left\| \gamma_i(t) * u_k(t) \right\|_2^2, \tag{12}$$

where $\gamma_i(\omega) = \frac{1}{\alpha(\omega-\omega_i)^2}$, $i = 1, 2, \ldots, k$.

(d) To ensure complete reconstruction of $s_{SCG}(t)$, the following constraint need to be imposed:

$$s_{SCG}(t) = u_k(t) + \sum_{i=1}^{k-1} u_i(t) + u_p(t) = u_k(t) + u_r(t). \tag{13}$$

Assume $k-1$ modes are known. The kth mode can be obtained by a constrained minimization problem as:

$$\begin{aligned} &\min_{u_k, \omega_k, u_r} \alpha J_1 + J_2 + J_3 \\ &s.t.\ s_{SCG}(t) = u_k(t) + u_r(t), \end{aligned} \tag{14}$$

where α is the balancing parameter among J_1, J_2, and J_3. The constrained minimization problem (14) can be transformed to an unconstrained problem by Lagrangian multipliers as:

$$\begin{aligned} \mathcal{L}(u_k, \omega_k, \lambda) &= \alpha J_1 + J_2 + J_3 + \left\| s_{SCG}(t) - \left[u_k(t) + u_r(t) \right] \right\|_2^2 \\ &+ \langle \lambda(t), s_{SCG}(t) - \left[u_k(t) + u_r(t) \right] \rangle, \end{aligned} \tag{15}$$

where λ is the Lagrangian multiplier, the quadratic penalty term is used to encourage reconstruction fidelity and improve the convergence performance.

The solution of problem (14) can be found as the saddle point of (15) using ADMM which leads to the iterates [41]:

$$\hat{u}_k^{n+1}(\omega) = \frac{\hat{s}_{SCG}(\omega) + \alpha^2 \left(\omega - \omega_k^n\right)^4 \hat{u}_k^n(\omega) + \hat{\lambda}(\omega)/2}{\left[1 + \alpha^2 \left(\omega - \omega_k^n\right)^4\right] \left[1 + 2\alpha \left(\omega - \omega_k^n\right)^2 + \sum_{i=1}^{k-1} \frac{1}{\alpha^2 \left(\omega - \omega_i^n\right)^4}\right]}, \tag{16}$$

$$\omega_k^{n+1} = \frac{\int_0^{f_s/2} \omega \left| \hat{u}_k^{n+1}(\omega) \right|^2 d\omega}{\int_0^{f_s/2} \left| \hat{u}_k^{n+1}(\omega) \right|^2 d\omega}, \tag{17}$$

$$\begin{aligned} \hat{\lambda}^{n+1}(\omega) = \hat{\lambda}^n(\omega) + \tau \Bigg[\hat{s}_{SCG}(\omega) - \Big(\hat{u}_k^{n+1}(\omega) + \\ \left[\frac{\alpha^2 \left(\omega - \omega_k^{n+1}\right)^4 \left(\hat{s}_{SCG}(\omega) - \hat{u}_k^{n+1}(\omega) - \sum_{i=1}^{k-1} \hat{u}_i(\omega) + \hat{\lambda}(\omega)/2 \right)}{1 + \alpha^2 \left(\omega - \omega_k^{n+1}\right)^4} \right] \\ - \frac{\sum_{i=1}^{k-1} \hat{u}_i(\omega)}{1 + \alpha^2 \left(\omega - \omega_k^{n+1}\right)^4} + \sum_{i=1}^{k-1} \hat{u}_i(\omega) \Big) \Bigg], \end{aligned} \tag{18}$$

with convergence criteria

$$\frac{\left\| \hat{u}_k^{n+1}(\omega) - \hat{u}_k^n(\omega) \right\|_2^2}{\left\| \hat{u}_k^n(\omega) \right\|_2^2} < \varepsilon_1, \tag{19}$$

$$|\sigma^2 - \frac{1}{T} \| s_{SCG}(t) - \sum_{i=1}^{k} u_i(t) \|_2^2 | / \sigma^2 < \varepsilon_2, \tag{20}$$

where u_k^n is the kth mode at nth step of update, ω_k^n is the central frequency, f_s is the sampling frequency, τ is the time-step of the dual ascent, ε_1, and ε_2 are the tolerance, σ^2 is the noise variance, respectively. The SVMD algorithm is summarized in Algorithm 1.

We emphasize that the quality or purity of the input signal has a significant impact on the effectiveness and efficiency of the decomposition method. A SCG signal purified with interference cancellation method reduces the number of modes than that of the raw SCG signal, because the contaminating interference and noise in the raw signal require additional modes to represent. Consequently, the computational cost will also be reduced significantly.

We compare the SCG signals before and after interference removal in terms of their decomposition results using SVMD; see Fig. 5 as an example calculated from b013 in the CEBS database. The decomposition sequences are aligned from low to high frequency. The time waveform of 11 IMFs of the b013 is plotted in Fig. 5(a), which stems from the raw SCG signal without the interference cancellation. Fig. 5(b) shows the counterpart after interference cancellation, which has only 7 IMFs, less than that of the raw SCG signal. The results verify the necessity of the interference cancellation.

We then exemplify the computational costs of VMD, SVMD before and after the interference cancellation in Fig. 6, where the number of modes of VMD is set to $K = 11$, the same that of the raw data processed by SVMD. Interference cancellation reduces the complexity of the subsequent SVMD. As a result, the follow-up heartbeat monitoring task can be achieved faster.

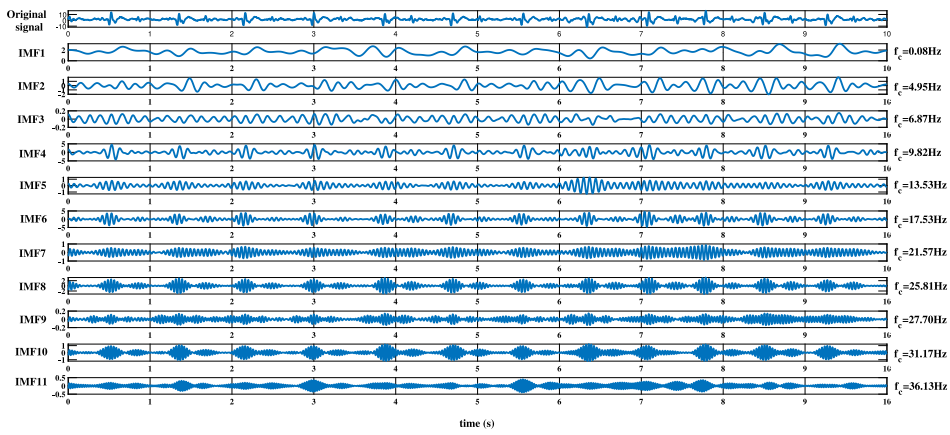

(a) IMFs from SVMD before interference cancellation

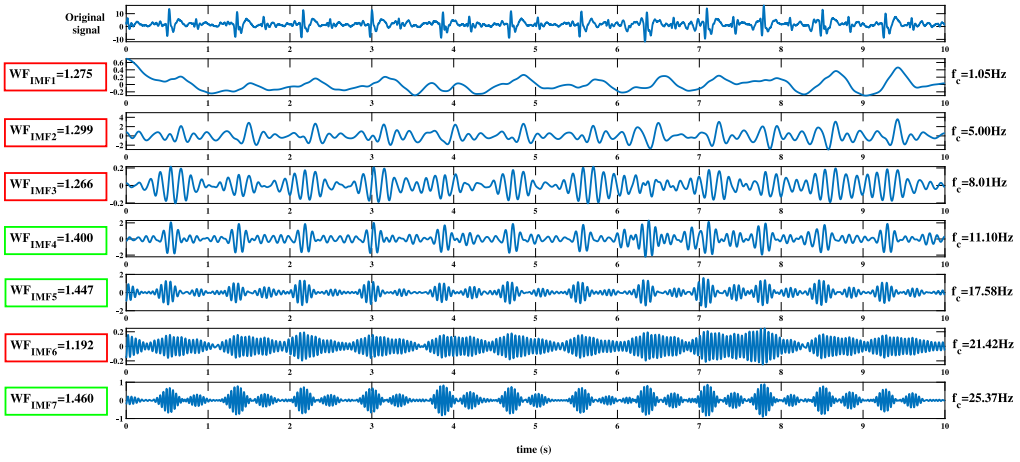

(b) IMFS from SVMD after interference cancellation

Fig. 5. Comparison of SVMD signal decomposition results for b013 before (a) and after (b) interference cancellation.

2.3.2. Signal screening criterion

Following signal decomposition, how to choose appropriate IMF components to reconstruct the AO signal of the various subject morphology is vital for accurately estimating the heartbeat cycle. Taking into account the pulsatile nature of the AO signal, we seek those IMFs with significant pulsatility. To this end, we propose a waveform-factor based method: We first use waveform factor defined in [56] to evaluate the pulsatile level of each IMF; Then, we select those IMFs which have higher pulsatile levels than average.

The waveform factor of the kth IMF is defined as [56]:

$$WF_k = \frac{\sqrt{\frac{1}{N}\sum_{t=1}^{N} u_k^2(t)}}{\frac{1}{N}\sum_{t=1}^{N} |u_k(t)|}, \tag{21}$$

where $u_k(t)$ denotes the kth IMF resulting from SVMD, and N denotes the number of samples of the 10 s predefined time interval. The waveform factor quantitatively characterizes the level of fluctuation. As for the IMF of a SCG signal, more significant fluctuation implies more significant pulsatility. As seen in Fig. 5(b), higher waveform factor values (green rectangles) indicate IMFs with more notable pulsation characters.

We then calculate the average as:

$$\alpha = \frac{1}{K}\sum_{k=1}^{K} WF_k, \tag{22}$$

and find those IMFs with waveform factors higher than the average. Denote their indices by:

$$m \in \{k | WF_k > \alpha, k = 1, 2, \ldots, K\}. \tag{23}$$

Based on the criterion, these IMF components are selected to reconstruct the AO signal; see (7) for details.

2.4. AO peak detection

With the reconstructed AO signal, we still need to extract and smooth the envelope, facilitating peak detection and the subsequent heart rate estimation. However, there are still some less significant peaks remaining in the AO signal, which will cause spurious detection.

Algorithm 1 SVMD

Input $s_{SCG}(t)$
Set α, ε_1, ε_2, and σ^2
Initialize, $k \leftarrow 0$
repeat
$k \leftarrow k+1$
Initialize $\hat{u}_k^1$, $\hat{\lambda}^1$, $\hat{\omega}_k^1$, $n \leftarrow 0$
repeat
$n \leftarrow n+1$
1) Update $\hat{u}_k$ for all $\omega > 0$:

$$\hat{u}_k^{n+1}(\omega) = \frac{\hat{s}_{SCG}(\omega)+\alpha^2\left(\omega-\omega_k^n\right)^4\hat{u}_k^n(\omega)+\hat{\lambda}(\omega)/2}{\left[1+\alpha^2\left(\omega-\omega_k^n\right)^4\right]\left[1+2\alpha\left(\omega-\omega_k^n\right)^2+\sum_{i=1}^{k-1}\frac{1}{\alpha^2\left(\omega-\omega_i^n\right)^4}\right]}$$

2) Update ω_k:

$$\omega_k^{n+1} = \frac{\int_0^{f_s/2}\omega\left|\hat{u}_k^{n+1}(\omega)\right|^2 d\omega}{\int_0^{f_s/2}\left|\hat{u}_k^{n+1}(\omega)\right|^2 d\omega}$$

3)Dual ascent for all $\omega \le 0$

$$\hat{\lambda}^{n+1}(\omega) = \hat{\lambda}^n(\omega) + \tau\left[\hat{s}_{SCG}(\omega) - \left(\hat{u}_k^{n+1}(\omega)+\left[\frac{\alpha^2\left(\omega-\omega_k^{n+1}\right)^4\left(\hat{s}_{SCG}(\omega)-\hat{u}_k^{n+1}(\omega)-\sum_{i=1}^{k-1}\hat{u}_i(\omega)+\hat{\lambda}(\omega)/2\right)}{1+\alpha^2\left(\omega-\omega_k^{n+1}\right)^4}\right]\right.\right.$$
$$\left.\left.-\frac{\sum_{i=1}^{k-1}\hat{u}_i(\omega)}{1+\alpha^2\left(\omega-\omega_k^{n+1}\right)^4}+\sum_{i=1}^{k-1}\hat{u}_i(\omega)\right)\right],$$

until convergence: $\frac{\left\|\hat{u}_k^{n+1}(\omega)-\hat{u}_k^n(\omega)\right\|_2^2}{\left\|\hat{u}_k^n(\omega)\right\|_2^2} < \varepsilon_1$
until convergence: $|\sigma^2 - \frac{1}{T}\|s_{SCG}(t) - \sum_{i=1}^{k}u_i(t)\|_2^2|/\sigma^2 < \varepsilon_2$

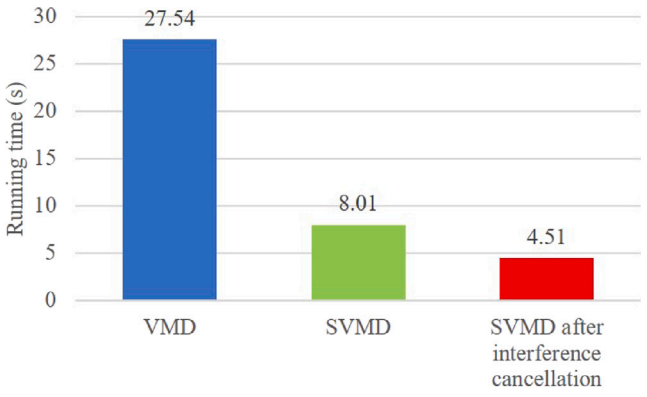

Fig. 6. Running time comparison. The duration of the tested signal is 10 s. All the experiments are implemented with Matlab 2018b on a PC with the 11th Gen Intel(R) Core(TM) i5-1135G7 CPU @ 2.40 GHz.

See Fig. 7(a) and (b) as an example. To remove these spurious peaks, we apply seventh power operation upon the AO signal prior to the envelope extraction, which yields a cleaner envelope. We then use window sliding for envelope smoothing, detailed in the following.

2.4.1. Seventh power law detection

Intuitively, the high-order (>2) power of the reconstructed AO signal magnifies the significant peaks while weakens the weak parts relatively, which enlarges the difference between the significant and weak parts in the signal. The theoretical analysis in [57] shows that as pulse duration decreases the order of the optimal power law should increase accordingly in order to improve the detection performance. Therefore, in the case of AO signal detection, of which the pulse duration is very short, a higher power law detector is preferable. Empirically, we find that the seventh power law detector well suppressed unwanted small peaks around the desired ones and achieved a higher detection probability, given by:

$$\tilde{s}_{AO}(t) = s_{AO}^7(t). \tag{24}$$

An example is given in Fig. 7(c) and (d). Compared to Fig. 7(a) and (b), the seventh power law detector yields a much cleaner envelope.

2.4.2. Envelope smoothing and AO peak detection

After the seventh power operation and obtaining the signal envelope by the Hilbert transformation [58], we further smooth the obtained envelope, in order to remove remaining spurious peaks [33]. This is achieved by a sliding average filter. Denote the envelope of $\tilde{s}_{AO}(t)$ by $s_{EN}(t)$. The average filter outputs the sliding local average to yield the smoothed envelope, given by

$$\bar{s}_{EN}(t) = \frac{1}{T}\sum_{i=t}^{t+T-1} s_{EN}(i), \tag{25}$$

where the window width T is empirically set to correspond to the duration of 1/10 s.

After envelope smoothing, the significant peaks are considered as the AO points. We illustrate the processing results over a raw SCG signal in Fig. 8. As shown in Fig. 8(b), the IMF components selected by the waveform factor criterion have a more significant peak at AO peak time. Fig. 8(c) shows that the AO peaks are highlighted by the seventh power law detector and other information is effectively suppressed. The results of Fig. 8(d) and (e) demonstrate that the AO peaks in the heartbeat cycle are more conspicuous after the envelope extraction and the moving average filtering. Finally, the position of the AO peak is determined by finding the main peak of the envelope.

2.5. Heart rate estimation

As can be seen from Fig. 8(e), the AO peaks appear periodically in the smoothed envelope. The AO-AO interval is considered as the instantaneous heart rate of the subject.

3. Experimental results and analysis

To verify the proposed method, we utilize the SCG data from a typical public dataset, i.e., CEBS [42]. The CEBS dataset contains ECG data, respiratory data and SCG data recorded from 20 healthy individuals using Biopac MP36 signal acquisition system, in which subjects were asked to lie awake on a comfortable single bed in a supine position. Firstly, about 5 min of the basal state data were measured (records b001 to b020). Subsequently, approximately 50 min data were collected while listening to classical music (records m001 to m020). Finally, about 5 min data were recorded after the music ended (records p001 to p020).

To reduce the computational cost, the original SCG signal is decimated by reducing the sampling rate from 5 KHz to 500 Hz. The CEBS database is diverse and representative, in which many cardiac activities and typical statuses were considered, e.g., narrower or wider systolic outline signals of SCG, sudden changes in cardiac amplitude, irregularity of cardiac rhythm, motion artifacts, trend effects, baseline drift, low AO amplitude [13,35].

Here, in order to correspond to the data in the Refs. [13,35], we only use first 200 s data for b001 to b020 in Tables 1 and 2, and then separate the data of 10 s as a segment to sequentially input them into the proposed method. More details on the results of all the data can be found in Tables 3–6.

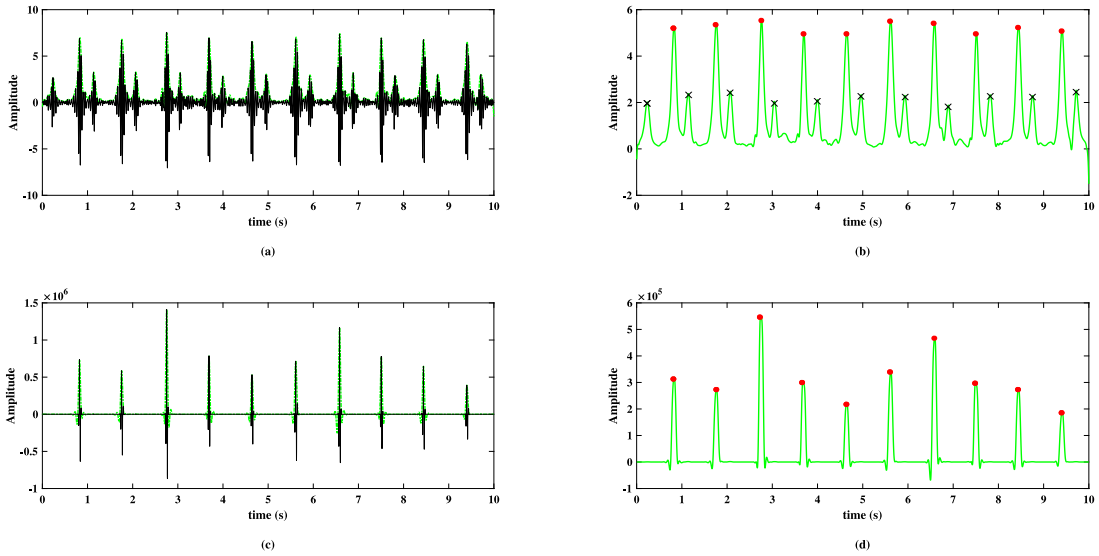

Fig. 7. Comparison between envelope extraction with and without seventh power law detection for b016. (a) Reconstructed signal (black) and envelope (green) without the seventh power detection, (c) the counterparts with the seventh power detection, (b) and (d) are peak detection results for (a) and (c), respectively. Red dots and black '×' denotes the AO peaks and spurious peaks, respectively.

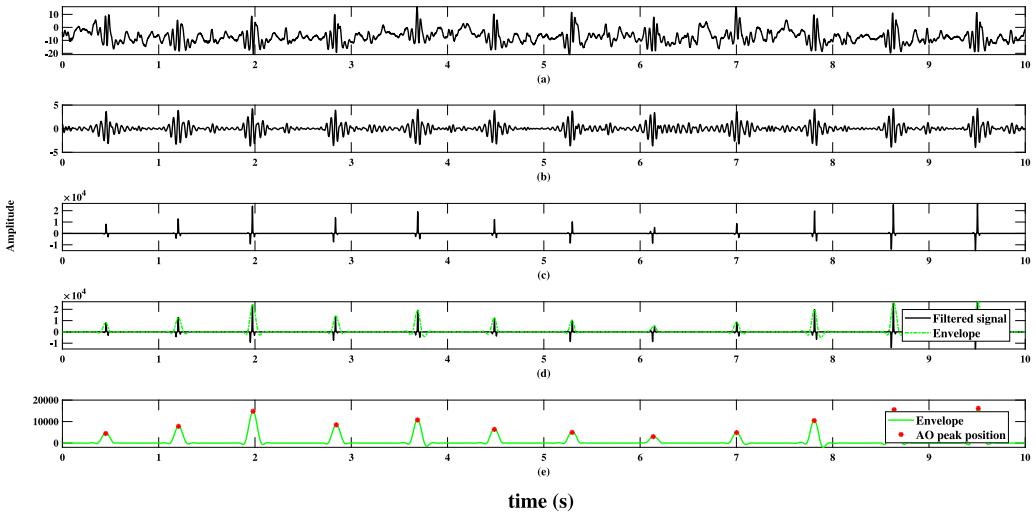

Fig. 8. An example of processing for b016. (a) Original SCG signal, $s(t)$ (b) reconstructed AO signal after preprocessing, SVMD and IMF selection, $s_{AO}(t)$, (c) seventh power law detection, $\bar{s}_{AO}(t)$, (d) envelop signal, $s_{EN}(t)$, and (e) smoothed envelope $\bar{s}_{EN}(t)$ and extracted AO peaks.

3.1. Overall performance

We consider four metrics, the detection error rate (DER), accuracy (ACC), sensitivity (SE), and peak accuracy (P), to evaluate the performance of the AO peak detection. The four metrics are defined as follows [35]:

$$\mathrm{DER} = \frac{\mathrm{FP}+\mathrm{FN}}{\mathrm{TP}+\mathrm{FN}} \times 100\%, \tag{26}$$

$$\mathrm{ACC} = \frac{\mathrm{TP}}{\mathrm{TP}+\mathrm{FP}+\mathrm{FN}} \times 100\%, \tag{27}$$

$$\mathrm{SE} = \frac{\mathrm{TP}}{\mathrm{TP}+\mathrm{FN}} \times 100\%, \tag{28}$$

$$\mathrm{P} = \frac{\mathrm{TP}}{\mathrm{TP}+\mathrm{FP}} \times 100\%, \tag{29}$$

where true-positive (TP), false-negative (FN), and false-positive (FP) denote that the AO peak is correctly identified, the AO peak is missing, and the AO peak is incorrectly identified due to the noise peak, respectively.

Table 1 summarizes the performance of the proposed method in terms of these four metrics. From Table 1, the proposed method can find the AO peak accurately even when several SCG signals change over time following noise and motion artifacts. It is noted that the CEBS dataset is diverse, in which some AO points are not the most prominent peak under certain circumstances and the amplitudes of other base point peaks are larger than that of the AO peak [13,35]. In other words, the whole SCG signal waveform may be relatively flat. However, even under such unfavorable factors, the proposed method can still yield good performance. Our technique produces 43 FPs and 45 FNs heartbeats out of a total of 4594 analyzed heartbeats with average sensitivity of 99.02%, average prediction rate of 99.06%, mean accuracy of 98.10%, and mean error rate of 1.92%. It should be noted that the performance of our technique is almost completely comparable to the performance of manual annotation in [59], in which the average sensitivity is 99.5% and the average prediction rate is 99.1%.

Moreover, the results of entire dataset from the proposed method are also available in Tables 3–5 for b001–b020, m001–m020, and p001–p020, respectively.

Table 1
Algorithm performance evaluation for signals in CEBS dataset (first 200 s of records b001 to b020).

Number	TP	FP	FN	Beats	DER (%)	SE (%)	P (%)	ACC (%)
b001	218	3	2	220	2.273	99.091	98.643	97.758
b002	205	1	0	205	0.488	100.000	99.515	99.515
b003	228	2	3	231	2.165	98.701	99.130	97.854
b004	217	0	0	217	0.000	100.000	100.000	100.000
b005	241	0	0	241	0.000	100.000	100.000	100.000
b006	205	2	0	205	0.976	100.000	99.034	99.034
b007	180	5	1	181	3.315	99.448	97.297	96.774
b008	316	0	0	316	0.000	100.000	100.000	100.000
b009	207	2	0	207	0.966	100.000	99.043	99.043
b010	205	1	0	205	0.488	100.000	99.515	99.515
b011	225	1	0	225	0.444	100.000	99.558	99.558
b012	269	0	1	270	0.370	99.630	100.000	99.630
b013	238	0	0	238	0.000	100.000	100.000	100.000
b014	228	0	1	229	0.437	99.563	100.000	99.563
b015	219	1	0	219	0.457	100.000	99.545	99.545
b016	238	0	0	238	0.000	100.000	100.000	100.000
b017	241	1	0	241	0.415	100.000	99.587	99.587
b018	255	4	13	268	6.343	95.149	98.456	93.750
b019	210	0	0	210	0.000	100.000	100.000	100.000
b020	204	20	24	228	19.298	89.474	91.071	82.258
Total	4549	43	45	4594	1.916	99.020	99.064	98.102
STD	–	–	–	–	4.37	2.44	1.94	3.94

Table 2
The proposed method is compared with previous peak detection methods (first 200 s of records b001 to b020).

Method	Test dataset	(#B;#S)	Performance
[43]	CEBS	– ; 20	SE: 98.5, P: 98.6, ACC: –
[13]	CEBS	4585; 20	SE: 94.3, P: 90.2, ACC: 85.6
[35]	CEBS	4585; 20	SE: 97.4, P: 97.4, ACC: 95.1
Proposed	CEBS	4594; 20	SE: 99.0, P: 99.1, ACC: 98.1

#B:Number of beats analyzed, #S: Number of subjects for data.
The unit of indicators such as SE, P and ACC is %. The sign "–" means that the corresponding value cannot be answered.

3.2. Comparison with other methods

Comparison between the proposed method and several state-of-the-art AO peak detection methods is provided in Table 2. It is worth mentioning that the corresponding performance metrics in [35] are the average sensitivity of 97.4%, the average prediction rate of 97.4%, the average accuracy rate of 95.1%, and mean error rate of 5.18%. Although both the proposed method and the method in [35] employ the signal decomposition method to extract IMFs, there is a main difference between them. Our approach combines two simple MTI filters to form a bandpass filter, which can remove both low frequency and high frequency artifacts at very low computational cost. After the interference cancellation, SVMD is employed to decompose the signal without specifying the number of modes. The method in [35] employs two stage VMD with specifying the number of modes, in which VMD in the first stage is used to remove low frequency artifacts at high computational cost. In addition, we use the waveform factor criterion to select the proper IMFs for the heartbeat signal reconstruction. Then, we design a seventh power law detector followed by the Hilbert transformation and moving average, since this facilitates to emphasize the AO peak. Moreover, it is observed that our technique is superior to [43] about 0.5%. The experimental results show that, the proposed method outperforms those counterparts in [13,35,43] on CEBS dataset across all performance metrics.

In addition, a comparison of the detection performance for all data between the proposed method and the method employed in [30] is shown in Table 6. It is interesting to note that the proposed method is about on average 10%, 5%, and 12% better than the method employed in [30] for b001–b020, m001–m020, and p001–p020, respectively.

Table 3
Algorithm performance evaluation of the entire data of records b001–b020.

Number	TP	FP	FN	Beats	DER (%)	SE (%)	P (%)	ACC (%)
b001	296	6	3	299	3.010	98.997	98.013	97.049
b002	308	1	0	308	0.325	100.000	99.676	99.676
b003	344	2	4	348	1.724	98.851	99.422	98.286
b004	325	1	0	325	0.308	100.000	99.693	99.693
b005	363	0	0	363	0.000	100.000	100.000	100.000
b006	310	2	0	310	0.645	100.000	99.359	99.359
b007	270	8	2	272	3.676	99.265	97.122	96.429
b008	480	0	0	480	0.000	100.000	100.000	100.000
b009	313	2	0	313	0.639	100.000	99.365	99.365
b010	309	3	0	309	0.971	100.000	99.038	99.038
b011	338	1	0	338	0.296	100.000	99.705	99.705
b012	404	0	1	405	0.247	99.753	100.000	99.753
b013	359	0	0	359	0.000	100.000	100.000	100.000
b014	344	0	1	345	0.290	99.710	100.000	99.710
b015	330	1	0	330	0.303	100.000	99.698	99.698
b016	352	0	0	352	0.000	100.000	100.000	100.000
b017	366	0	0	366	0.000	100.000	100.000	100.000
b018	383	5	17	400	5.500	95.750	98.711	94.568
b019	316	0	0	316	0.000	100.000	100.000	100.000
b020	304	31	34	338	19.231	89.941	90.746	82.385
Total	6814	63	62	6876	1.818	99.098	99.084	98.199
STD	–	–	–	–	4.34	2.31	2.04	3.90

Table 4
Algorithm performance evaluation of the entire data of records m001–m020.

Number	TP	FP	FN	Beats	DER (%)	SE (%)	P (%)	ACC (%)
m001	3065	40	18	3083	1.881	99.416	98.712	98.143
m002	3235	7	0	3235	0.216	100.000	99.784	99.784
m003	3432	167	18	3450	5.362	99.478	95.360	94.885
m004	3407	28	0	3407	0.822	100.000	99.185	99.185
m005	3561	14	33	3594	1.308	99.082	99.608	98.697
m006	3107	17	9	3116	0.834	99.711	99.456	99.170
m007	2615	38	0	2615	1.453	100.000	98.568	98.568
m008	4998	2	19	5017	0.419	99.621	99.960	99.582
m009	3161	17	0	3161	0.538	100.000	99.465	99.465
m010	2988	330	1	2989	11.074	99.967	90.054	90.027
m011	3597	0	2	3599	0.056	99.944	100.000	99.944
m012	3983	2	4	3987	0.150	99.900	99.950	99.850
m013	3708	2	4	3712	0.162	99.892	99.946	99.838
m014	3394	9	24	3418	0.965	99.298	99.736	99.037
m015	3205	2	0	3205	0.062	100.000	99.938	99.938
m016	3859	0	3	3862	0.078	99.922	100.000	99.922
m017	3517	71	71	3588	3.958	98.021	98.021	96.119
m018	3587	1	0	3587	0.028	100.000	99.972	99.972
m019	3197	3	0	3197	0.094	100.000	99.906	99.906
m020	3364	13	35	3399	1.412	98.970	99.615	98.593
Total	68 980	763	241	69 221	1.450	99.652	98.906	98.565
STD	–	–	–	–	2.63	0.51	2.34	2.4

3.3. Comparison with ECG

In this subsection, we compare the results from the proposed method for SCG with the counterpart of ECG. Fig. 9 shows the R wave of ECG as the gold reference for the detected actual AO peak position. Incidentally, Fig. 9 also reveals the time delay between the R peak and the AO peak. Fig. 10 shows an example of AO-AO and R–R gap diagram of the b016 subject in order to illustrate the reliability of the method. These results demonstrate that the AO peak position yielded by the proposed method can match up with the ECG reference.

To further show the reliability of our approach, the instantaneous heart rate from SCG is also compared with the instantaneous heart rate obtained from the ECG data in the CEBS dataset. Four commonly used statistical metrics, Mean, average value relative error (ARE), average absolute error (AAE), and average absolute error percentage (AAEP), are used to measure the error between the measured value and the reference value [60,61]. The last three indicators are defined as follows:

$$\mathrm{ARE} = \frac{\left|\mathrm{SCG}_{\mathrm{ave}} - \mathrm{ECG}_{\mathrm{ave}}\right|}{\mathrm{ECG}_{\mathrm{ave}}}, \tag{30}$$

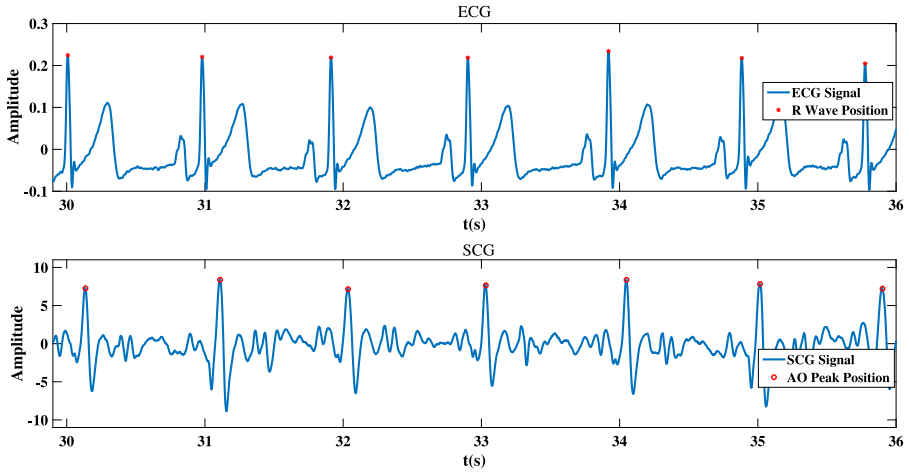

Fig. 9. Detection results of SCG via the proposed method. (a) Reference from ECG, (b) AO peak positions (red dots) for SCG of b016 via our technique.

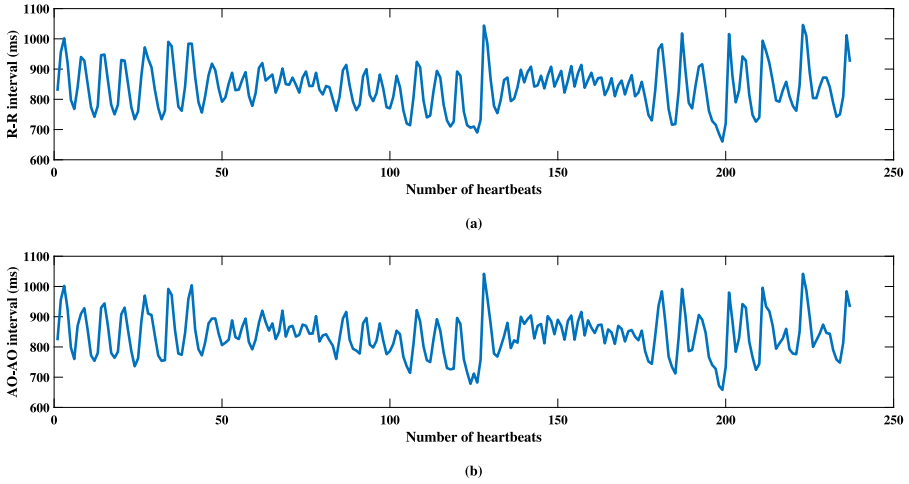

Fig. 10. R–R gaps graph of ECG (above) and AO–AO gaps graph of SCG (below) for b016 subject.

Table 5
Algorithm performance evaluation of the entire data of records p001–p020.

Number	TP	FP	FN	Beats	DER (%)	SE (%)	P (%)	ACC (%)
p001	324	7	1	325	2.462	99.692	97.885	97.590
p002	308	1	0	308	0.325	100.000	99.676	99.676
p003	344	2	4	348	1.724	98.851	99.422	98.286
p004	324	2	0	324	0.617	100.000	99.387	99.387
p005	363	0	0	363	0.000	100.000	100.000	100.000
p006	310	2	0	310	0.645	100.000	99.359	99.359
p007	272	6	0	272	2.206	100.000	97.842	97.842
p008	474	0	6	480	1.250	98.750	100.000	98.750
p009	313	2	0	313	0.639	100.000	99.365	99.365
p010	309	3	0	309	0.971	100.000	99.038	99.038
p011	338	1	0	338	0.296	100.000	99.705	99.705
p012	403	1	1	404	0.495	99.752	99.752	99.506
p013	359	0	0	359	0.000	100.000	100.000	100.000
p014	341	4	4	345	2.319	98.841	98.841	97.708
p015	330	1	0	330	0.303	100.000	99.698	99.698
p016	352	0	0	352	0.000	100.000	100.000	100.000
p017	366	1	0	366	0.273	100.000	99.728	99.728
p018	385	4	15	400	4.750	96.250	98.972	95.297
p019	316	0	0	316	0.000	100.000	100.000	100.000
p020	333	3	5	338	2.367	98.521	99.107	97.654
Total	6864	40	36	6900	1.101	99.478	99.421	98.905
STD	–	–	–	–	1.22	0.93	0.64	1.21

Table 6
The proposed method is compared with previous peak detection methods for the entire data.

Test dataset	Method	(#B;#S)	Performance
b001–b020	[30]	6873;20	SE: 89.3, P: 89.6
b001–b020	Proposed	6876;20	SE: 99.1, P: 99.1
m001–m020	[30]	70217;20	SE: 93.9, P: 94.5
m001–m020	Proposed	69221;20	SE: 99.7, P: 98.9
p001–p020	[30]	6864;20	SE: 87.7, P: 85.7
p001–p020	Proposed	6900;20	SE: 99.5, P: 99.4

#B:Number of beats analyzed, #S: Number of subjects for data. The unit of indicators of SE and P is %.

$$\mathrm{AAE} = \frac{1}{N}\sum_{n=1}^{N}\left|\mathrm{SCG}_{\mathrm{est}}(n) - \mathrm{ECG}_{\mathrm{ref}}(n)\right|, \tag{31}$$

$$\mathrm{AAEP} = \frac{1}{N}\sum_{n=1}^{N}\left|\frac{\mathrm{SCG}_{\mathrm{est}}(n) - \mathrm{ECG}_{\mathrm{ref}}(n)}{\mathrm{ECG}_{\mathrm{ref}}(n)}\right|, \tag{32}$$

where $\mathrm{SCG}_{\mathrm{ave}}$, $\mathrm{ECG}_{\mathrm{ave}}$ denote the average value of SCG and ECG, respectively. N, $\mathrm{SCG}_{\mathrm{est}}(n)$, and $\mathrm{ECG}_{\mathrm{ref}}(n)$ denote the total number of heart rate monitors, the nth SCG instantaneous heart rate, and ECG reference values, respectively.

As shown in Table 7, the instantaneous heart rate from SCG obtained by the proposed method is almost exactly identical to that of ECG. As an example, the results of the corresponding correlation and

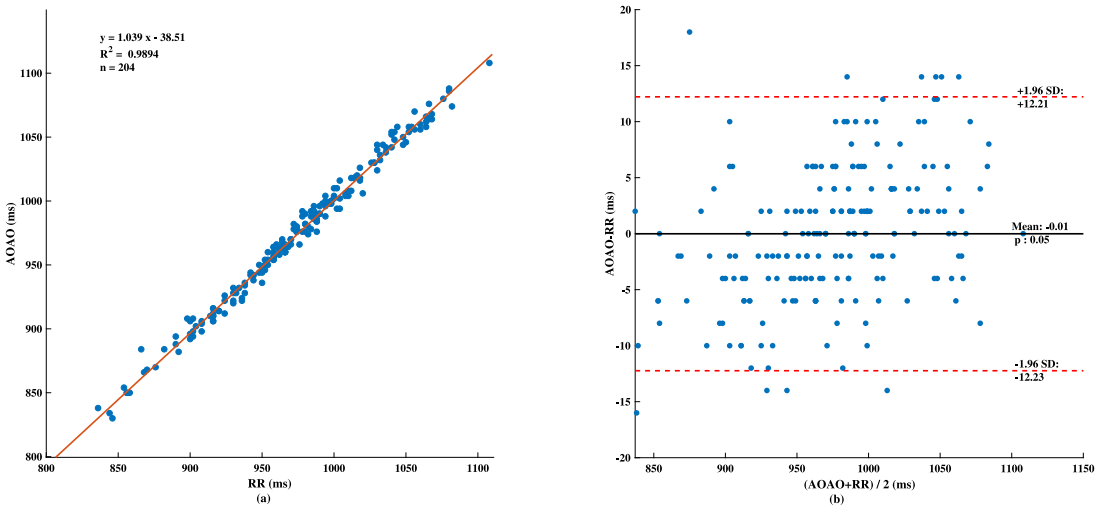

Fig. 11. Statistical analyses on beat–beat intervals obtained form ECG and SCG for a total of 204 heartbeats of b002. (a) Linear correlation (b) Bland–Altman analysis. The analyses are performed on R–R and AO–AO intervals using Matlab toolbox "cftool".

Table 7
Comparison between SCG measurement results and ECG reference values.

Number	ECG mean	SCG mean	ARE	AAE	AAEP (%)
b001	66.18	67.43	0.01884	–	–
b002	61.87	61.96	0.00150	0.4773	0.7730
b003	69.45	70.22	0.01109	–	–
b004	65.67	65.61	0.00098	0.6166	0.9189
b005	72.34	72.37	0.00042	1.3003	1.7892
b006	61.88	62.67	0.01277	0.8606	0.0136
b007	54.45	56.26	0.03317	–	–
b008	95.45	95.67	0.00230	0.8663	0.9083
b009	62.33	63.39	0.01711	1.0055	0.0147
b010	61.72	61.79	0.00120	1.1325	1.8289
b011	68.08	68.12	0.00057	0.8426	1.2309
b012	81.10	81.01	0.00103	1.4806	1.7973
b013	72.03	72.13	0.00145	1.1529	1.5850
b014	69.10	68.80	0.00433	1.4771	2.1119
b015	66.06	66.02	0.00065	0.6653	1.0062
b016	72.92	72.74	0.00242	1.0171	1.3972
b017	72.61	72.59	0.00020	0.3510	0.4852
b018	81.63	79.53	0.02566	–	–
b019	63.05	63.05	0.00001	0.8936	1.4256
b020	68.50	68.22	0.00411	–	–

The sign "–" means that the corresponding value cannot be answered. The reason is that the amounts of R–R and AO–AO heartbeat do not match due to relatively large FPs and FNs. As for b002, b015, b017 the match can be achieved by removing only one FP point.

Table 8
Bland–Altman Analysis of records b001 to b020.

Number	mean	mean + 1.96 sd	mean − 1.96 sd	Limits of agreement	R^2
b001	–	–	–	–	–
b002	−0.01	12.21	−12.23	95%	0.9894
b003	–	–	–	–	–
b004	0.10	23.75	−23.55	95%	1.0000
b005	0.10	32.11	−31.91	95%	1.0000
b006	0.06	42.05	−41.93	95%	1.0000
b007	–	–	–	–	–
b008	0.18	30.30	−29.94	95%	1.0000
b009	−1.11	78.00	−80.23	95%	1.0000
b010	−0.07	19.79	−19.93	95%	1.0000
b011	−0.79	105.29	−106.87	95%	1.0000
b012	−0.37	20.00	−20.75	95%	1.0000
b013	0.03	58.24	−58.17	95%	1.0000
b014	0.25	72.20	−71.71	95%	1.0000
b015	−1.40	63.73	−66.53	95%	1.0000
b016	−0.03	25.77	−25.82	95%	1.0000
b017	0.03	8.03	−7.96	95%	1.0000
b018	–	–	–	–	–
b019	−0.69	45.67	−47.05	95%	1.0000
b020	–	–	–	–	–

The sign "–" means that the corresponding value cannot be answered. The reason is that the amounts of R–R and AO–AO heartbeat do not match due to relatively large FPs and FNs.

Bland–Altman analyses for b002 are shown in Fig. 11.[1] These analyses show that a slope and intercept of 1.04 and −38.51 ms with R^2 values of 0.99 and a bias of −0.01 ms ($p = 0.05$) with limits of agreement of (−12.23; 12.21) ms. This example further demonstrates that our technique can yield accurate heart rate via the acceleration sensor without ECG as a reference. Our approach can be extended to a variety of platforms for real-time and reliable assessment of heart rate.

4. Conclusion

In this paper, a high accurate AO peaks detection method is proposed for SCG without reference to the R wave of the ECG. We construct a first order bandpass filter that is a combination of two simple MTI filters to cancel out-band artifacts for the raw output signal of the accelerometer. Due to the purified SCG signal with reduced number of modes, the computational burden of the signal decomposition stage can be effectively reduced. Further, SVMD that does not require the prior knowledge of the number of modes is employed to decompose the purified SCG signal at a low computational cost. The waveform factor criterion induced from the pulsatile nature of the AO signal is utilized to select the subbands with possible AO peaks for AO signal reconstruction. Subsequently, a seventh power law detector is designed to enlarge the contrast between the amplitude of AO peaks and the remaining non-AO peaks, yielding a much cleaner envelope for AO peak detection. The proposed method achieves an average SE of 99.02%, an average P of 99.06%, and an average ACC of 98.10% approximately over 4594 analyzed beats for public CEBS database. The results clearly show that our approach outperforms several state-of-the-art methods. In addition, estimates of the instantaneous heart rate of the proposed method from SCG and the ECG's instantaneous heart rate are also a good match. Future work is to detect abnormal cardiac activity in

[1] The Bland–Altman results of records b001 to b020 are shown in Table 8.

patients by evaluating the discriminative characteristics in SCG based on transfer learning similar to [62,63].

CRediT authorship contribution statement

Chundi Zheng: Conceptualization, Methodology, Formal analysis, Writing – reviewing & editing. **Weiming Peng:** Data curation, Writing – original draft, Validation. **Tianyao Huang:** Writing – reviewing & editing, Methodology. **Yonina C. Eldar:** Writing – reviewing & editing. **Meiyi Yu:** Validation, Investigation, Formal analysis.

Declaration of competing interest

The authors declare that they have no known competing financial interests or personal relationships that could have appeared to influence the work reported in this paper.

Data availability

We utilize the SCG data from a typical public dataset, i.e., CEBS.

References

[1] WHO, Global Status Report on Noncommunicable Diseases 2014, World Health Organization, 2014.

[2] The Writing Committee of the Report on Cardiovascular Health and Diseases in China, Summary of China cardiovascular health and disease report 2019, Chin. Circ. J. 39 (10) (2020) 1157–1162.

[3] E.J. Benjamin, P. Muntner, A. Alonso, M.S. Bittencourt, C.W. Callaway, et al., Heart disease and stroke statistics-2019 update: A report from the American heart association, Circulation 139 (2019) e56–e528.

[4] D. Rai, H.K. Thakkar, S.S. Rajput, J. Santamaria, C. Bhatt, F. Roca, A comprehensive review on seismocardiogram: current advancements on acquisition, annotation, and applications, Mathematics 9 (18) (2021) 2243.

[5] U.R. Acharya, P. Joseph, N. Kannathal, C. Lim, J. Suri, Heart rate variability: A review, Med. Biol. Eng. Comput. 44 (2007) 1031–1051.

[6] J.M. Zanetti, K. Tavakolian, Seismocardiography: Past, present and future, in: 35th Annual International Conference of the IEEE Engineering in Medicine and Biology Society (EMBC), 2013, pp. 7004–7007.

[7] M. Jafari Tadi, E. Lehtonen, A. Saraste, J. Tuominen, J. Koskinen, M. Teräs, J. Airaksinen, M. Pänkäälä, T. Koivisto, Gyrocardiography: A new non-invasive monitoring method for the assessment of cardiac mechanics and the estimation of hemodynamic variables, Sci. Rep. 7 (1) (2017) 1–11.

[8] A. Hossein, J. Rabineau, D. Gorlier, J.I.J. Del Rio, P. Van De Borne, P.-F. Migeotte, A. Nonclercq, Kinocardiography derived from ballistocardiography and seismocardiography shows high repeatability in healthy subjects, Sensors 21 (3) (2021) 815.

[9] E. Andreozzix, G.D. Gargiulo, D. Esposito, P. Bifulco, A novel broadband forcecardiography sensor for simultaneous monitoring of respiration, infrasonic cardiac vibrations and heart sounds, Front. Physiol. (2021) 1988.

[10] E. Andreozzi, A. Fratini, D. Esposito, G. Naik, C. Polley, G.D. Gargiulo, P. Bifulco, Forcecardiography: A novel technique to measure heart mechanical vibrations onto the chest wall, Sensors 20 (14) (2020) 3885.

[11] E. Andreozzi, J. Centracchio, D. Esposito, P. Bifulco, A comparison of heart pulsations provided by forcecardiography and double integration of seismocardiogram, Bioengineering 9 (4) (2022) 167.

[12] F. Santucci, D. Lo Presti, C. Massaroni, E. Schena, R. Setola, Precordial vibrations: A review of wearable systems, signal processing techniques, and main applications, Sensors 22 (15) (2022) 5805.

[13] T. Choudhary, L.N. Sharma, M.K. Bhuyan, Automatic detection of aortic valve opening using seismocardiography in healthy individuals, IEEE J. Biomed. Health Inf. 23 (3) (2019) 1032–1040.

[14] R. Crow, P. Hannan, D. Jacobs Jr, L. Hedquist, D. Salerno, Relationship between seismocardiogram and echocardiogram for events in the cardiac cycle, Am. J. Noninvasive Cardiol. 8 (1) (1994) 39–46.

[15] M.J. Tadi, E. Lehtonen, T. Hurnanen, J. Koskinen, J. Eriksson, M. Pänkäälä, M. Teräs, T. Koivisto, A real-time approach for heart rate monitoring using a Hilbert transform in seismocardiograms, Physiol. Meas. 37 (11) (2016) 1885–1909.

[16] C. Yang, N. Tavassolian, Motion artifact cancellation of seismocardiographic recording from moving subjects, IEEE Sens. J. 16 (14) (2016) 5702–5708.

[17] Y. D'Mello, J. Skoric, S. Xu, P.J.R. Roche, M. Lortie, S. Gagnon, D.V. Plant, Real-time cardiac beat detection and heart rate monitoring from combined seismocardiography and gyrocardiography, Sensors 19 (16) (2019).

[18] J. Centracchio, E. Andreozzi, D. Esposito, G.D. Gargiulo, P. Bifulco, Detection of aortic valve opening and estimation of pre-ejection period in forcecardiography recordings, Bioengineering 9 (3) (2022) 89.

[19] O.T. Inan, P.-F. Migeotte, K.-S. Park, M. Etemadi, K. Tavakolian, R. Casanella, J. Zanetti, J. Tank, I. Funtova, G.K. Prisk, M. Di Rienzo, Ballistocardiography and seismocardiography: A review of recent advances, IEEE J. Biomed. Health Inf. 19 (4) (2015) 1414–1427.

[20] A. Taebi, B.E. Solar, A.J. Bomar, R.H. Sandler, H.A. Mansy, Recent advances in seismocardiography, Vibration 2 (1) (2019) 64–86.

[21] M.J. Tadi, E. Lehtonen, T. Koivisto, M. Pänkäälä, A. Paasio, M. Teräs, Seismocardiography: Toward heart rate variability (HRV) estimation, in: IEEE International Symposium on Medical Measurements and Applications (MeMeA), 2015, pp. 261–266.

[22] T. Choudhary, M. Das, L. Sharma, M.K. Bhuyan, Analyzing seismocardiographic approach for heart rate variability measurement, Biomed. Signal Process. Control 68 (2021) 102793.

[23] D. Rai, H.K. Thakkar, S.S. Rajput, Performance characterization of binary classifiers for automatic annotation of aortic valve opening in seismocardiogram signals, in: 9th International Conference on Bioinformatics and Biomedical Science (ICBBE), 2020.

[24] J. Centracchio, S. Parlato, D. Esposito, P. Bifulco, E. Andreozzi, ECG-free heartbeat detection in seismocardiography signals via template matching, Sensors 23 (10) (2023) 4684.

[25] N. Mora, F. Cocconcelli, G. Matrella, P. Ciampolini, Fully automated annotation of seismocardiogram for noninvasive vital sign measurements, IEEE Trans. Instrum. Meas. 69 (4) (2020) 1241–1250.

[26] F. Khosrow-khavar, K. Tavakolian, A.P. Blaber, J.M. Zanetti, R. Fazel-Rezai, C. Menon, Automatic annotation of seismocardiogram with high-frequency precordial accelerations, IEEE J. Biomed. Health Inf. 19 (4) (2015) 1428–1434.

[27] M. Jafari Tadi, T. Koivisto, M. Pänkäälä, A. Paasio, Accelerometer-based method for extracting respiratory and cardiac gating information for dual gating during nuclear medicine imaging, Int. J. Biomed. Imaging 2014 (2014) 690124.

[28] J. Vertens, F. Fischer, C. Heyde, F. Höflinger, R. Zhang, L. Reindl, A. Gollhofer, Measuring respiration and heart rate using two acceleration sensors on a fully embedded platform, in: 3rd International Congress on Sport Sciences Research and Technology Support, 2015, pp. 15–23.

[29] C. Yang, S. Tang, N. Tavassolian, Utilizing gyroscopes towards the automatic annotation of seismocardiograms, IEEE Sens. J. 17 (7) (2017) 2129–2136.

[30] S. Siecinski, E.J. Tkacz, P.S. Kostka, Comparison of HRV indices obtained from ECG and SCG signals from CEBS database, Biomed. Eng. Online 18 (2019) 1–15.

[31] Q. Chen, X. Lang, L. Xie, H. Su, Multivariate intrinsic chirp mode decomposition, Signal Process. 183 (2021) 108009.

[32] S. Siecinski, P.S. Kostka, E.J. Tkacz, Influence of empirical mode decomposition on heart rate variability indices obtained from smartphone seismocardiograms, in: 41st Annual International Conference of the IEEE Engineering in Medicine and Biology Society (EMBC), 2019, pp. 4913–4916.

[33] T. Choudhary, L.N. Sharma, M.K. Bhuyan, Standalone heartbeat extraction in SCG signal using variational mode decomposition, in: International Conference on Wireless Communications, Signal Processing and Networking (WiSPNET), 2018, pp. 1–4.

[34] K. Dragomiretskiy, D. Zosso, Variational mode decomposition, IEEE Trans. Signal Process. 62 (3) (2014) 531–544.

[35] T. Choudhary, M.K. Bhuyan, L.N. Sharma, A novel method for aortic valve opening phase detection using SCG signal, IEEE Sens. J. 20 (2) (2020) 899–908.

[36] C.-S. Chen, Y. Jeng, Nonlinear data processing method for the signal enhancement of GPR data, J. Appl. Geophys. 75 (1) (2011) 113–123.

[37] Y. Yaslan, B. Bican, Empirical mode decomposition based denoising method with support vector regression for time series prediction: A case study for electricity load forecasting, Measurement 103 (2017) 52–61.

[38] B. Erfianto, A. Rizal, V. Suryani, Comparison of seismocardiography based heart rate measurement method, J. Southwest Jiaotong Univ. 55 (6) (2020) 1–15.

[39] C. Will, P. Vaishnav, A. Chakraborty, A. Santra, Human target detection, tracking, and classification using 24-GHz FMCW radar, IEEE Sens. J. 19 (17) (2019) 7283–7299.

[40] P. Nallabolu, L. Zhang, H. Hong, C. Li, Human presence sensing and gesture recognition for smart home applications with moving and stationary clutter suppression using a 60-GHz digital beamforming FMCW radar, IEEE Access 9 (2021) 72857–72866.

[41] M. Nazari, S.M. Sakhaei, Successive variational mode decomposition, Signal Process. (2020).

[42] A. Goldberger, L. Amaral, L. Glass, J. Hausdorff, P. Ivanov, R. Mark, J. Mietus, G. Moody, C. Peng, H. Stanley, PhysioBank, PhysioToolkit, and PhysioNet: components of a new research resource for complex physiologic signals, Circulation (2000).

[43] F. Cocconcelli, N. Mora, G. Matrella, P. Ciampolini, High-accuracy, unsupervised annotation of seismocardiogram traces for heart rate monitoring, IEEE Trans. Instrum. Meas. 69 (9) (2020) 6372–6380.

[44] Y. D'Mello, J. Skoric, S. Xu, Autocorrelated differential algorithm for real-time seismocardiography analysis, IEEE Sens. J. 19 (13) (2019) 5127–5140.

[45] D.J. Lin, J.P. Kimball, J. Zia, V.G. Ganti, O.T. Inan, Reducing the impact of external vibrations on fiducial point detection in seismocardiogram signals, IEEE Trans. Biomed. Eng. 69 (1) (2022) 176–185.

[46] M. Haescher, D.J. Matthies, J. Trimpop, B. Urban, A study on measuring heart-and respiration-rate via wrist-worn accelerometer-based seismocardiography (SCG) in comparison to commonly applied technologies, in: 2nd International Workshop on Sensor-Based Activity Recognition and Interaction, 2015, pp. 1–6.
[47] G. Shafiq, S. Tatinati, K.C. Veluvolu, Automatic annotation of peaks in seismocardiogram for systolic time intervals, in: 8th Annual International Conference of the IEEE Engineering in Medicine and Biology Society (EMBC), IEEE, 2016, pp. 2672–2675.
[48] C. Yang, N.D. Aranoff, P. Green, N. Tavassolian, Classification of aortic stenosis using time–frequency features from chest cardio-mechanical signals, IEEE Trans. Biomed. Eng. 67 (6) (2019) 1672–1683.
[49] T. Hurnanen, E. Lehtonen, M.J. Tadi, Automated detection of atrial fibrillation based on time–frequency analysis of seismocardiograms, IEEE J. Biomed. Health Inf. 21 (5) (2017) 1233–1241.
[50] F. Cocconcelli, N. Mora, G. Matrella, P. Ciampolini, High-accuracy, unsupervised annotation of seismocardiogram traces for heart rate monitoring, IEEE Trans. Instrum. Meas. 69 (9) (2020) 6372–6380.
[51] M. Skolnik, Radar Handbook, third ed., McGraw-Hill, New York, 2008.
[52] S. Thanagasundram, F.S. Schlindwein, Comparison of integrated micro-electrical-mechanical system and piezoelectric accelerometers for machine condition monitoring, J. Mech. Eng. Sci. 220 (8) (2006) 1135–1146.
[53] J.D. Cryer, K.-S. Chan, Time Series Analysis with Applications in R, second ed., Springer, 2008.
[54] S. Boyd, N. Parikh, E. Chu, B. Peleato, J. Eckstein, et al., Distributed optimization and statistical learning via the alternating direction method of multipliers, Found. Trends® Mach. Learn. 3 (1) (2011) 1–122.
[55] Z. Mo, Z. Zhang, K.-L. Tsui, The variational kernel-based 1-D convolutional neural network for machinery fault diagnosis, IEEE Trans. Instrum. Meas. 70 (2021) 1–10.
[56] X. Miao, L. Zou, Z. Song, X. Wang, J. Wang, B. Liu, Study on PD pattern recognition of power transformer considering external corona interference signal, in: IEEE International Conference on High Voltage Engineering and Application (ICHVE), 2020, pp. 1–4.
[57] J.A. Fawcett, B.H. Maranda, The optimal power law for the detection of a Gaussian burst in a background of Gaussian noise, IEEE Trans. Inform. Theory 37 (1) (1991) 209–214.
[58] A.V. Oppenheim, J.R. Buck, R.W. Schafer, Discrete-Time Signal Processing, second ed., Prentice Hall, 1999.
[59] S. Siecinski, P.S. Kostka, E.J. Tkacz, Heart rate variability analysis on CEBS database signals, in: 40th Annual International Conference of the IEEE Engineering in Medicine and Biology Society (EMBC), 2018, pp. 5697–5700.
[60] C. Ye, K. Toyoda, T. Ohtsuki, Improved sparse adaptive algorithms for accurate non-contact heartbeat detection using time-window-variation technique, in: 40th Annual International Conference of the IEEE Engineering in Medicine and Biology Society (EMBC), 2018, pp. 1–6.
[61] S. Wang, A. Pohl, T. Jaeschke, M. Czaplik, M. Köny, S. Leonhardt, N. Pohl, A novel ultra-wideband 80 GHz FMCW radar system for contactless monitoring of vital signs, in: 37th Annual International Conference of the IEEE Engineering in Medicine and Biology Society (EMBC), 2015, pp. 4978–4981.
[62] S. Lu, Z. Zhang, Y. Zhang, S. Wang, CGENet: A deep graph model for COVID-19 detection based on chest CT, Biology 11 (1) (2022) 33.
[63] S. Lu, S. Wang, Y. Zhang, Detection of abnormal brain in MRI via improved AlexNet and ELM optimized by chaotic bat algorithm, Neural Comput. Appl. 33 (2021) 10799–10811.